Supporting Information

Composition-Dependent Hydrogen-Bonding Motifs and Dynamics in Brønsted Acid-Base Mixtures

Christian Malm, Leon A. Prädel, Bogdan A. Marekha, Maksim Grechko, Johannes Hunger*

Max-Planck-Institute for Polymer Research, Ackermannweg 10, 55128 Mainz, Germany.

*Email: hunger@mpip-mainz.mpg.de

Table of Contents

Fourier transform infrared spectra

Figure S1 shows linear infrared (IR) spectra of Qu and DPP dissolved in dichloromethane (DCM) in a broader frequency range. Two bands at 2040 cm^{-1} and 2500 cm^{-1} and a minor band at about 3400 cm^{-1} have been related to the intermolecular hydrogen-bonds between Qu and DPP (A,B,C-type pattern[1,2]).

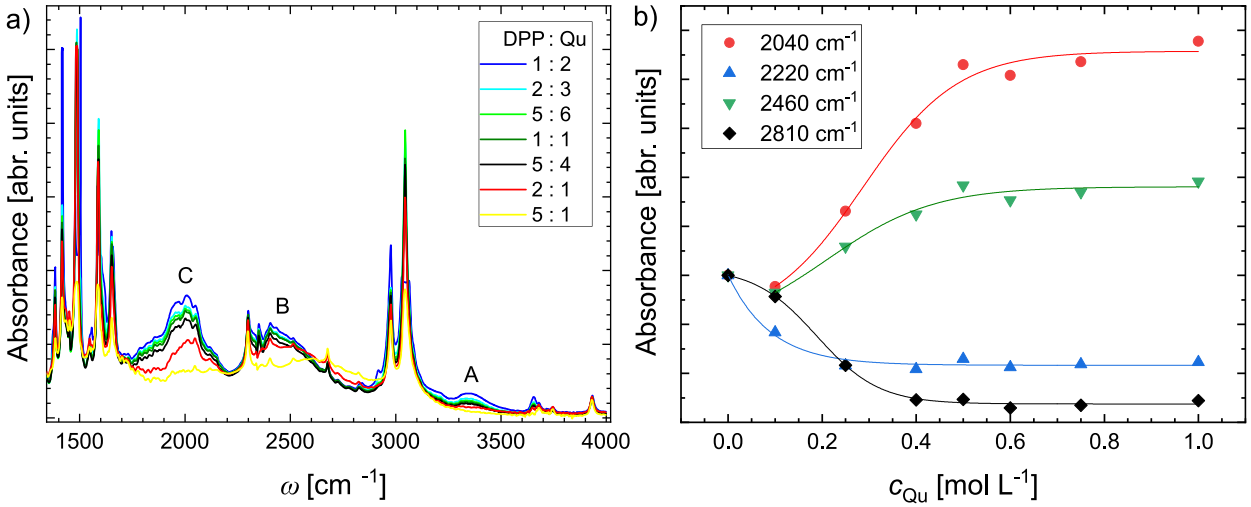

Figure S1: a) FTIR spectra of Qu and DPP mixtures in DCM. All solutions contain 0.5 mol L^{-1} Qu with varying DPP concentration (1, 0.75, 0.6, 0.5, 0.4, 0.25, and 0.1 mol L^{-1}). b) Infrared absorbance of DPP-Qu mixtures (normalized to 1 at c_{Qu}=0 mol L^{-1}) at selected frequencies as a function of c_{Qu}. Symbols are experimental data, lines are mere guides to the eye. Upon addition of Qu, spectral intensity at blue-shifted frequencies (2810 cm^{-1}) decreases, while the absorbance at 2460 cm^{-1} and 2040 cm^{-1} increases. Hence the overall spectral intensity red-shifts, except for the absorption at 2220 cm^{-1}, where a spectral minimum appears with increasing concentration of Qu.

Decomposition of the infrared spectra

In order to disentangle the individual contributions of quinaldine (Qu), diphenyl phosphoric acid (diphenyl phosphate, DPP), ion-pairs (IP) and multimers (M) to the Fourier-transformed infrared (FTIR) spectra (Figure 2b in the main manuscript), we decompose the solvent subtracted FTIR spectra, shown in Figure 2a in the main text. Based on the formation constants reported previously,[3] we determine the equilibrium concentrations of ion-pairs ([*IP*]), multimers ([*M*]), 'free' quinaldine ([*Qu*]), and diphenyl phosphoric acid ([*DPP*]) using eqs S1 – S4 from the analytical Qu and DPP concentrations (c_{Qu} and c_{DPP}). We used the previously reported equilibrium constants for ion-pair and multimer formation ($K_1 = 104$ L mol^{-1} ; $K_2 = 16$ L mol^{-1}) for Qu and DPP in dichloromethane (DCM).[3] Here we approximate multimers by trimers.

$$c_{\mathrm{Qu}} = [Qu] + [IP] + [M] \tag{S1}$$

$$c_{\mathrm{DPP}} = [DPP] + [IP] + 2 \cdot [M] \tag{S2}$$

$$K_1 = \frac{[IP]}{[Qu] + [DPP]} \tag{S3}$$

$$K_2 = \frac{[M]}{[IP] + [DPP]} \tag{S4}$$

Figure S2a shows the resulting concentration profiles. With increasing Qu concentration, the amount of free DPP decreases and IPs are the dominating species in mixtures with a low DPP to Qu ratio.

The calculated concentration profiles were used to perform a least-squares solution with known covariance, with the concentrations of Figure S2a as covariances. The component spectra using four components describe the experimental spectra very well (see Figure S2b).

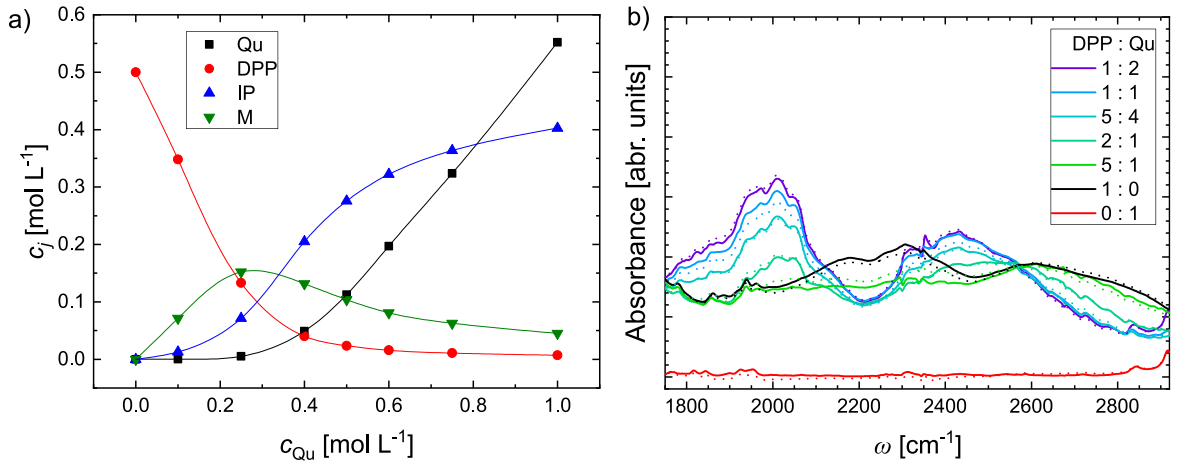

Figure S2: a) Calculated concentrations (symbols) of each individual component, which are used to calculate their individual spectral contributions to the FTIR spectra. In b) the resulting spectra using the concentration weighted sum of the four components (dotted lines) are compared to the experimental spectra (solid lines).

Density functional theory calculations

All calculations were performed using Gaussian 16[4] (B3LYP-D3(BJ)/6-31G(d) level of theory[5–7]) applying a polarizable continuum model[8] (dichloromethane) and Grimme's D3 dispersion with Becke-Johnson damping[9]. We note that the used basis set suffices to describe the proton transfer potential, yet for an accurate description of the vibrational coordinates involving the heavy phosphorous atom, a higher basis set would be required.[10] Fig. S3 shows the optimized geometries of a) the ion-pair, b) the DPP···DPP homo dimer, and c) the negatively charged DPP···DPP$^-$ homo dimer with Lithium as counter ion.

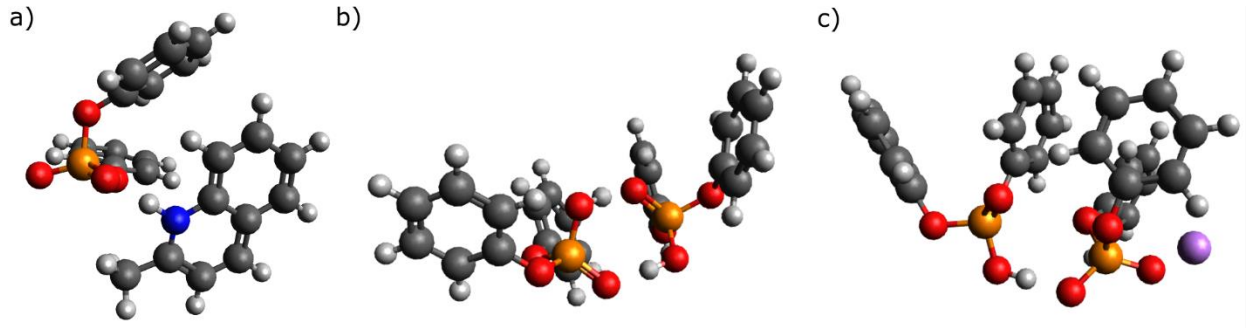

Figure S3: Optimized geometry for a) a doubly ionic hydrogen bonded DPP-Qu ion-pair, b) the DPP homo dimer and c) the negatively charged DPP···DPP$^-$ homo dimer with Lithium as counter ion.

The potentials shown in Fig. 3 of the main manuscript were obtained from a non-relaxed potential energy surface scan, starting from the optimized geometry and varying the N-H distance along the N-O axis of the doubly ionic hydrogen bond (or O-O axis for DPP dimers). Note that in the optimized geometry the hydrogen bonds are not perfectly linear, instead the IP has a HNO angle of 3.6°, the DPP homo dimer has an HOO angle of 6.0°, and the negatively charged DPP···DPP$^-$ homo dimer has an HOO angle of 0.6°.

In order to estimate vibrational transition frequencies of the N$^+$-H···O$^-$ and O-H···O stretching mode we calculated the energies of the three lowest lying eigenstates taking the potential energy as a function of the proton displacement along N-O/O-O bond vector. To this end, we have approximated the potential energy obtained on a 0.05 Å grid from a non-relaxed energy scan (see above) with a quartic function describing an asymmetric double well potential (similar to the function employed by Tokmakoff et al.[11]):

$$U(x) = \mu * (x - x_0)^4 - \kappa * (x - x_0)^2 + \beta * (x - x_0) + y_0 \qquad \text{(S5)}$$

The values of the fitted parameters and their explanation are given in the table S1.

Table S1: Parameters obtained from fitting eq. S5 to the potentials in Fig. 3 of the main manuscript.

Parameter	Fit result			Description
	$QuH^+\cdots DPP^-$	$DPP\cdots DPP$	$Li^+\cdots DPP^-\cdots DPP$	
μ, $cm^{-1}/Å^4$	286000 ± 4000	323000 ± 5000	338000 ± 4000	quartic parameter that controls the potential steepness at the edges
κ, $cm^{-1}/Å^2$	35000 ± 800	30500 ± 1000	27700 ± 800	quadratic parameter that controls the barrier height and steepness
β, $cm^{-1}/Å$	7300 ± 100	11200 ± 100	7800 ± 100	linear parameter that controls the asymmetry of the potential (inequivalence of the two wells)
x_0, Å	1.355 ± 0.001	1.301 ± 0.001	1.286 ± 0.001	center of the potential
y_0, cm^{-1}	2990 ± 30	3440 ± 40	2280 ± 20	offset

The obtained potential function was used to construct the Hamiltonian matrix within discrete variable representation (DVR) using the 'particle in a box' eigenfunctions as basis.[12] The reduced mass was assumed to be the proton mass. The eigenvalues of the Hamiltonian matrix were used to calculate the transition frequencies between the corresponding eigenstates shown in Fig. 3 in the main text.

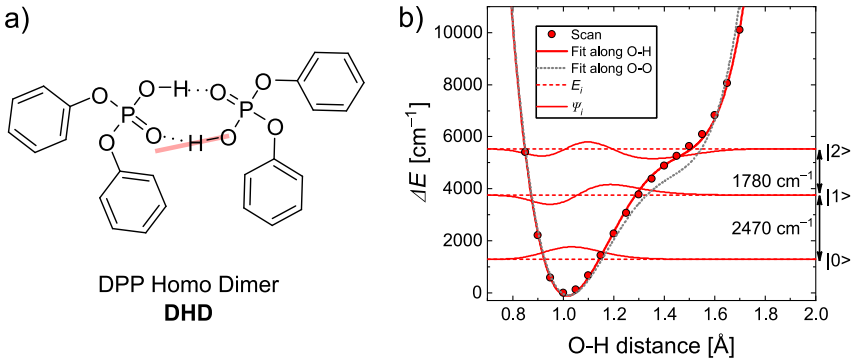

Figure S4 a) shows a schematic of the optimized geometry for DPP homo dimers, with an OOH angle of 6°. In b) the potential corresponding to the proton displacement along the OH axis of the optimized geometry is shown, which results in a |0> to |1> transition energy of 2470 cm^{-1}. The potential for proton displacement along the O-O axis is shown as grey dots for comparison.

To estimate the effect of the bond angle, we compare the transition frequency difference of a scan along the O-H axis of the optimized geometry to the potential along the O-O axis for a DPP homodimer, which differ by ~160 cm^{-1}.

Diagonal cut of the 2D-IR spectrum

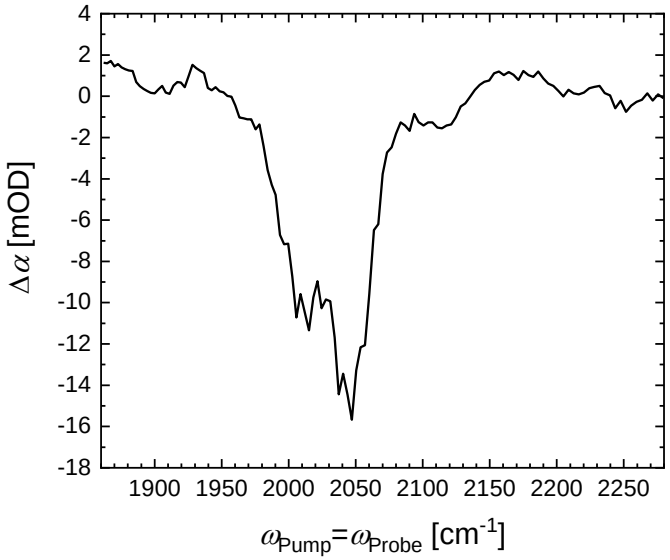

Figure S5: Cut along the diagonal for the 2D-IR spectrum of a 1:1 mixture of DPP and Qu at t = 50 fs, (Fig. 4b of the main text), which exhibits two main bleaching signals at ~2010 cm^{-1} and ~2040 cm^{-1}.

Transient IR experiments on DPP in DCM

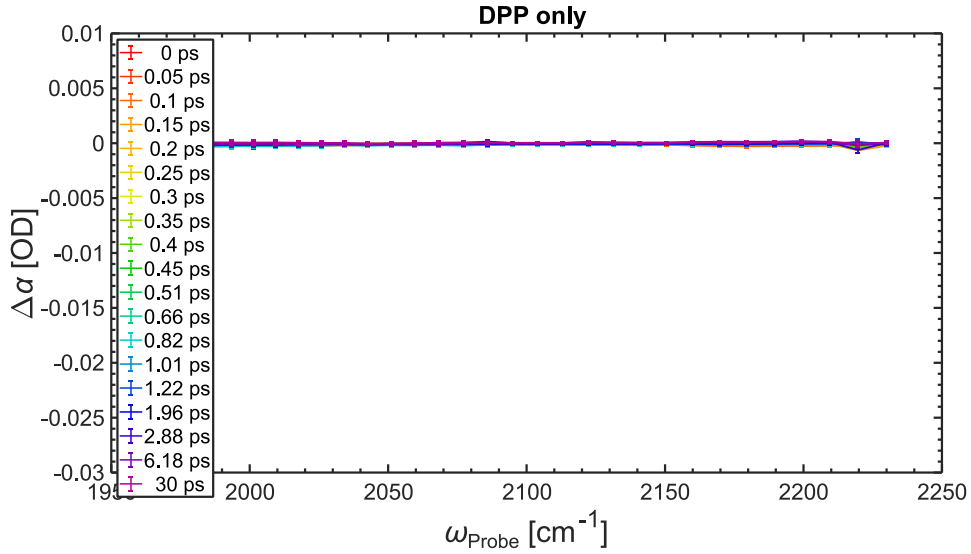

Figure S6: Transient IR spectra of 0.5 mol L^{-1} DPP in DCM exhibit no detectable signals. All other experimental parameters are the same as for the experiments shown in Fig. 6a of the main manuscript.

Transient IR experiments on Qu + DPP in DCM at 2500 cm^{-1}

Figure S7 shows the transient IR spectra of different DPP-Qu mixtures in DCM with the pump and probe pulses centered at ~2500 cm^{-1}. With increasing Qu concentration, the maximum bleaching signal shifts to lower frequencies, similar to the IR absorption peak (Figure S1). The transient absorption spectra are fitted with the same three state relaxation model as the transient absorption data measured at 2040 cm^{-1} (Fig. 6 of the main manuscript). The thus obtained relaxation times (Figure S8) exhibit the same variation with Qu concentration as the data shown in Fig. 6c of the main manuscript. The fast component (~100 fs) agrees well with the results shown in Fig. 6 of the main manuscript. The slower relaxation time is slower for experiments at ~2500 cm^{-1}, as compared to the experiments at 2000 cm^{-1}, which may indicate different relaxation pathways. The similarity of the relaxation at 2500 cm^{-1} and at 2040 cm^{-1} supports the notion that both frequency ranges have a common molecular origin (separated by the Evans hole[2,13,14]).

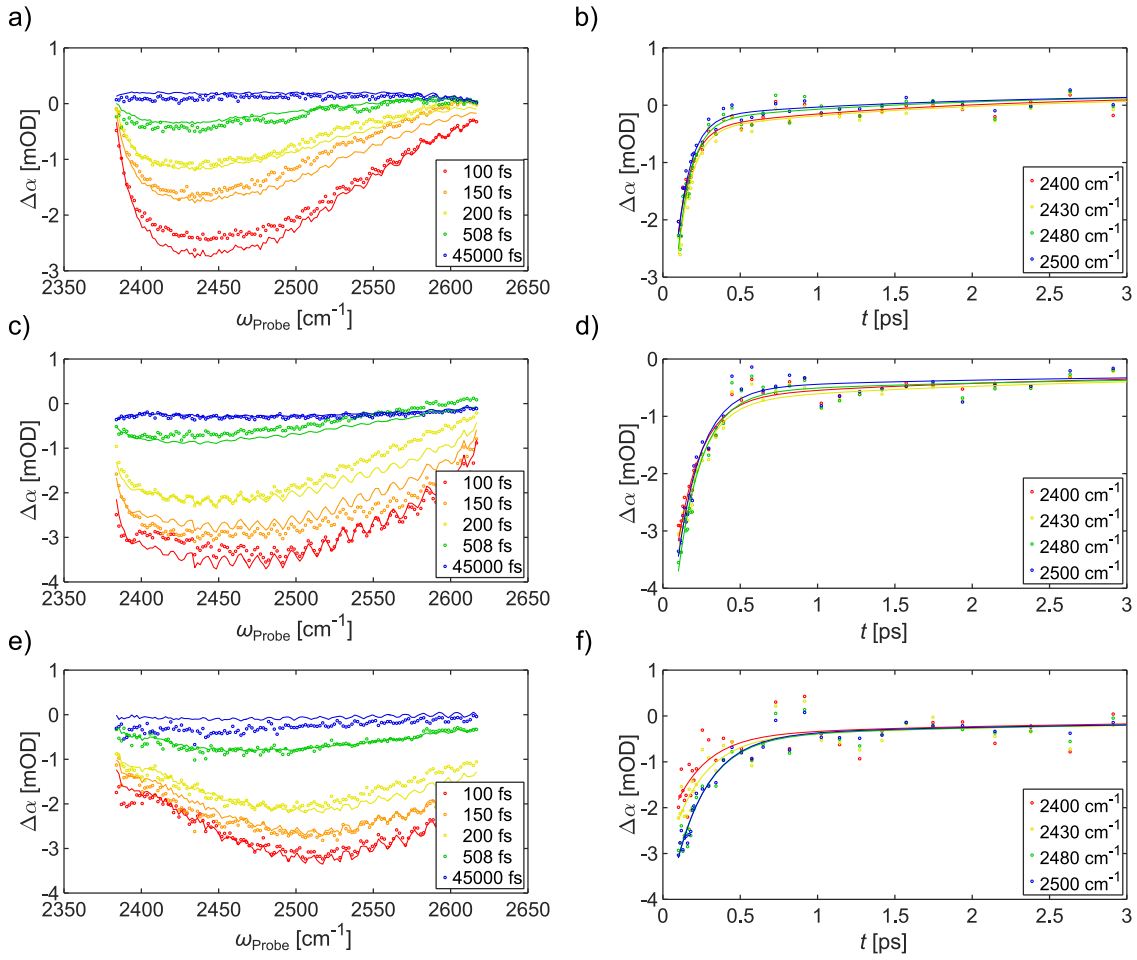

Figure S7: Transient IR experiments on mixtures of Qu and DPP in DCM at ~2500 cm^{-1}. The DPP concentration is kept constant at 0.5 mol L^{-1}, while c_{Qu} decreases from top to bottom: (a) & (b) 0.75 mol L^{-1}. (c) & (d) 0.5 mol L^{-1}, and (e) & (f) 0.25 mol L^{-1}. For both, transient spectra (a, c, e) and time traces (b, d, f), symbols represent experimental data and lines the fits with the three state kinetic model (see text below).

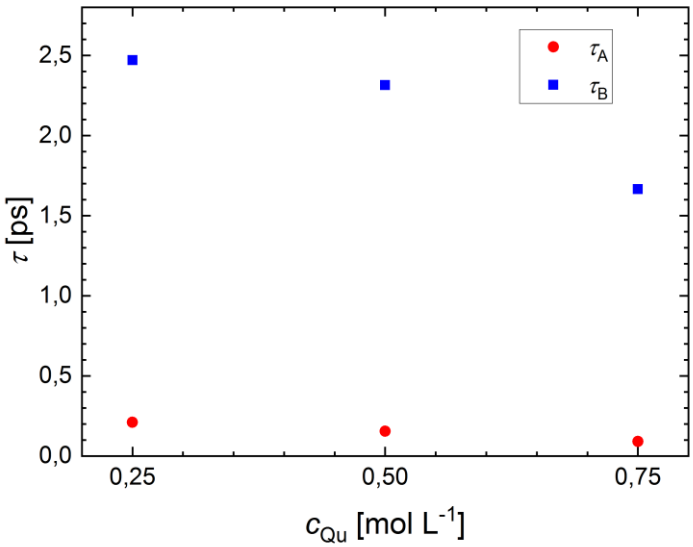

Figure S8: Relaxation times obtained from fitting the three state kinetic model to the data in Figure S7.

Transient IR experiments on Qu + DPP in DCM at 2000 cm^{-1}

Figure S9 shows the transient IR data of Qu and DPP mixtures in DCM at 2000 cm^{-1} at varying concentration of Qu together with the fits using the kinetic model to obtain the relaxation times shown in Fig. 6c of the main text.

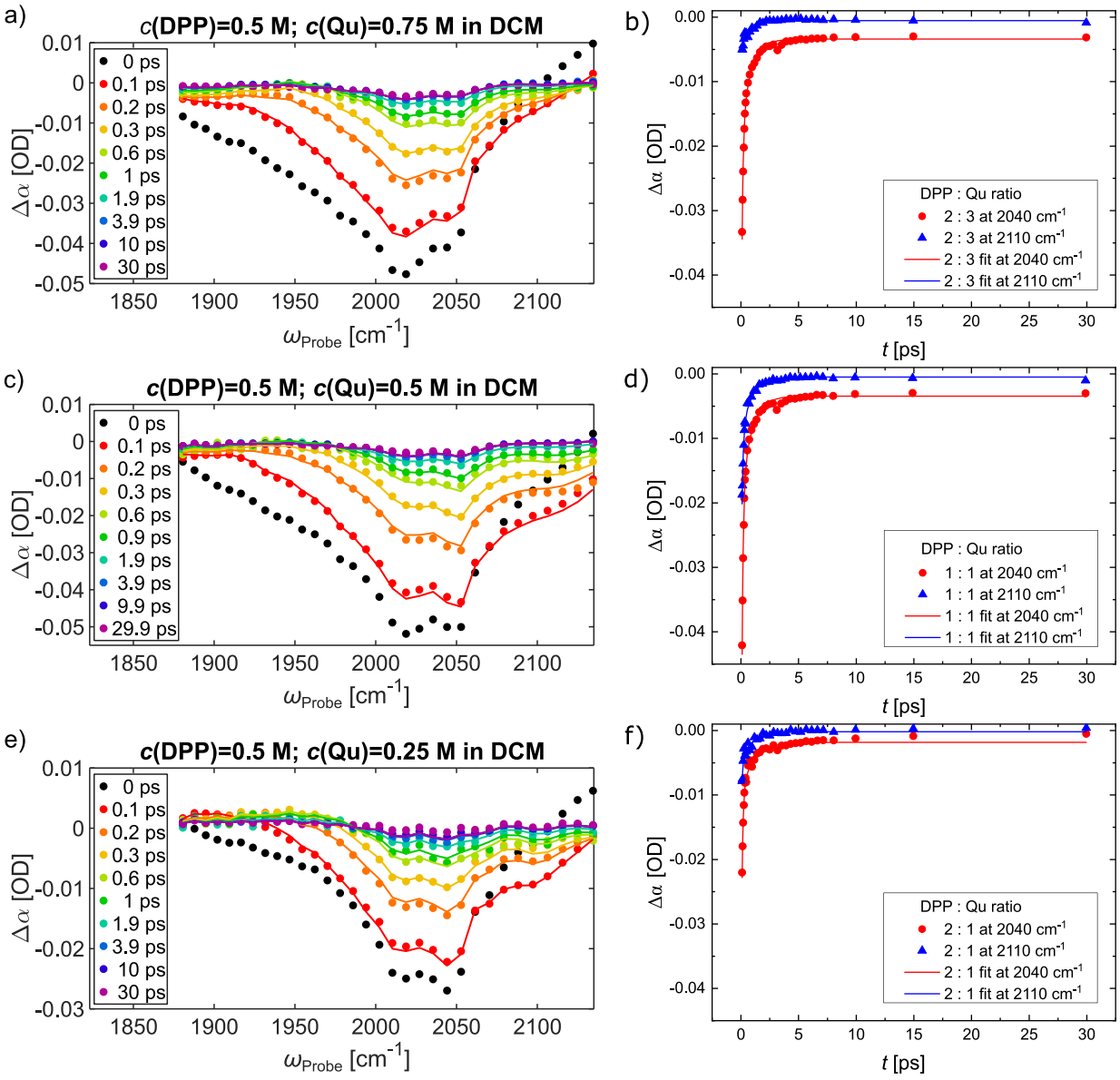

Figure S9: Transient infrared spectra and delay traces at selected probing frequencies for DPP:Qu mixtures at molar ratios 2:3 (a-b), at 1:1 (c-d), and 2:1 (e-f). Symbols show experimental data and lines show the fits with the kinetic model.

Kinetic Modelling

We use a three state kinetic model to describe all transient infrared experiments (see Figure 6c). In this model the excited state **1*** relaxes with τ_A to the intermediate state **0'** and subsequently with τ_B to the heated ground state **0''**. To obtain the time-dependent populations of **1*** (N_1), of **0'** ($N_{0'}$), and of **0''** ($N_{0''}$), we solve eqs (S6-S8):[15]

$$\frac{dN_1}{dt} = -\frac{1}{\tau_A} N_1 \tag{S6}$$

$$\frac{dN_{0'}}{dt} = \frac{1}{\tau_A} N_1 - \frac{1}{\tau_B} N_{0'} \tag{S7}$$

$$\frac{dN_{0''}}{dt} = \frac{1}{\tau_B} N_{0'} \tag{S8}$$

The transient spectra are modelled using the time dependent populations of the three states multiplied by the spectra of each component:

$$\Delta\alpha(\omega, t) = N_1(t)\sigma_1(\omega) + N_{0'}(t)\sigma_{0'}(\omega) + N_{0''}(t)\sigma_{0''}(\omega) \tag{S9}$$

The spectra associated with the three states ($\sigma_1(\omega)$, $\sigma_{0'}(\omega)$, and $\sigma_{0''}(\omega)$), obtained by fitting the model to the data in Figure S9, are displayed in Figure S10.

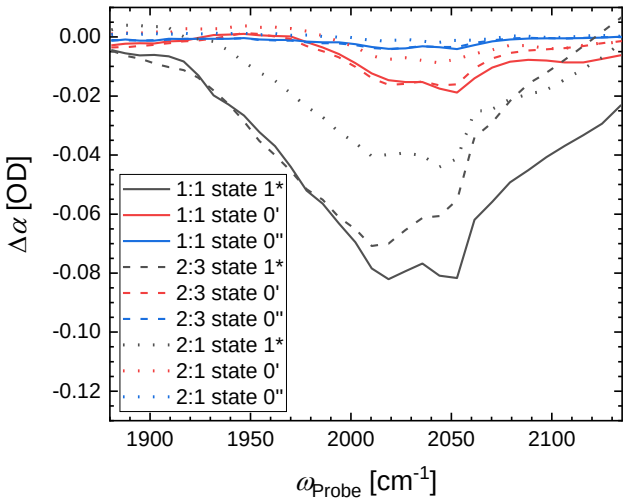

Figure S10: Spectra of the excited state, the intermediate state, and the heated ground state obtained by fitting the kinetic model to the experimental spectra for solutions at different DPP:Qu ratios (1:1, 2:3, and 2:1).

Supporting References

(1) Hadži, D. Infrared Spectra of Strongly Hydrogen-Bonded Systems. *Pure Appl. Chem.* **1965**, *11*, 435-453.

(2) Hadži, D. Spectroscopic and Structural Aspects of Very Strong Hydrogen Bonds. *Chimia.* **1972**, *26*, 7-13.

(3) Malm, C.; Kim, H.; Wagner, M.; Hunger, J. Complexity in Acid-Base Titrations: Multimer Formation Between Phosphoric Acids and Imines. *Chem. - A Eur. J.* **2017**, *23*, 10853–10860.

(4) Frisch, M. J.; Trucks, G. W.; Schlegel, H. B.; Scuseria, G. E.; Robb, M. A.; Cheeseman, J. R.; Scalmani, G.; Barone, V.; Petersson, G. A.; Nakatsuji, H. .et al *Gaussian 16 B.01*; Gaussian, Inc.: Wallingford CT, 2016.

(5) Becke, A. D. Density-Functional Thermochemistry. III. The Role of Exact Exchange. *J. Chem. Phys.* **1993**, *98*, 5648-5652.

(6) Petersson, G. A.; Bennett, A.; Tensfeldt, T. G.; Al-Laham, M. A.; Shirley, W. A.; Mantzaris, J. A Complete Basis Set Model Chemistry. I. The Total Energies of Closed-shell Atoms and Hydrides of the First-row Elements. *J. Chem. Phys.* **1988**, *89*, 2193–2218.

(7) Petersson, G. A.; Al-Laham, M. A. A Complete Basis Set Model Chemistry. II. Open-shell Systems and the Total Energies of the First-row Atoms. *J. Chem. Phys.* **1991**, *94*, 6081–6090.

(8) Scalmani, G.; Frisch, M. J. Continuous Surface Charge Polarizable Continuum Models of Solvation. I. General Formalism. *J. Chem. Phys.* **2010**, *132*, 114110.

(9) Grimme, S.; Ehrlich, S.; Goerigk, L. Effect of the Damping Function in Dispersion Corrected Density Functional Theory. *J. Comput. Chem.* **2011**, *32*, 1456–1465.

(10) Costard, R.; Tyborski, T.; Fingerhut, B. P. Anharmonicities and Coherent Vibrational Dynamics of Phosphate Ions in Bulk H_2O. *Phys. Chem. Chem. Phys.* **2015**, *17*, 29906–29917.

(11) Fournier, J. A.; Carpenter, W. B.; Lewis, N. H. C.; Tokmakoff, A. Broadband 2D IR Spectroscopy Reveals Dominant Asymmetric $H_5O_2^+$ Proton Hydration Structures in Acid Solutions. *Nat. Chem.* **2018**, *10*, 932–937.

(12) Colbert, D. T.; Miller, W. H. A Novel Discrete Variable Representation for Quantum Mechanical Reactive Scattering via the S-matrix Kohn Method. *J. Chem. Phys.* **1992**, *96*, 1982–1991.

(13) Bratos, S. Profiles of Hydrogen Stretching IR Bands of Molecules with Hydrogen Bonds: A Stochastic Theory. I. Weak and Medium Strength Hydrogen Bonds. *J. Chem. Phys.* **1975**, *63*, 3499–3509.

(14) Van Hoozen, B. L.; Petersen, P. B. Vibrational Tug-of-War: The pKa Dependence of the Broad Vibrational Features of Strongly Hydrogen-Bonded Carboxylic Acids. *J. Chem. Phys.* **2018**, *148*, 134309.

(15) Rezus, Y. L. A.; Bakker, H. J. On the Orientational Relaxation of HDO in Liquid Water. *J. Chem. Phys.* **2005**, *123*, 114502.